THE JOURNAL OF PHYSICAL CHEMISTRY LETTERS
A JOURNAL OF THE AMERICAN CHEMICAL SOCIETY

pubs.acs.org/JPCL

Letter

Quantitative Microscale Thermometry in Droplets Loaded with Gold Nanoparticles

Lucas Sixdenier,* Guillaume Baffou, Christophe Tribet, and Emmanuelle Marie*

Cite This: *J. Phys. Chem. Lett.* 2023, 14, 11200−11207

Read Online

ACCESS | Metrics & More | Article Recommendations | Supporting Information

ABSTRACT: Gold nanoparticles (AuNPs) are increasingly used for their thermoplasmonic properties, i.e., their ability to convert light energy into heat through plasmon resonance. However, measuring temperature gradients generated at the microscale by assemblies of AuNPs remains challenging, especially for random 3D distributions of AuNPs. Here, we introduce a label-free thermometry approach, combining quantitative wavefront microscopy and numerical simulations, to infer the heating power dissipated by a 3D model system consisting of emulsion microdroplets loaded with AuNPs. This approach gives access to the temperature reached in the droplets under laser irradiation without the need for extrinsic calibration. This versatile thermometry method is promising for noninvasive temperature measurements in various 3D microsystems involving AuNPs as colloidal heat sources, including photothermal drug delivery systems.

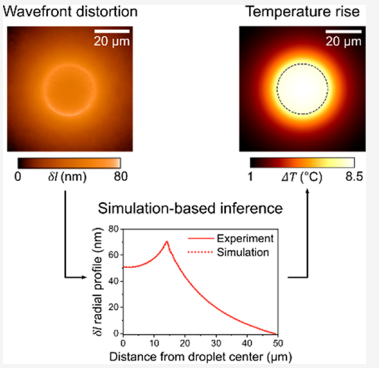

A local variation of temperature is a common trigger in a variety of stimuli-responsive systems that are for instance developed for targeted, controlled delivery of active loads, such as drugs,[1] or for on-demand actuation or a switch of material properties.[2,3] Remote stimulation and spatiotemporal control of heat dissipation may be obtained via the application of ultrasounds, magnetic fields, or light.[4,5] Noble metal nanoparticles, including the nontoxic gold nanoparticles (AuNPs), have sparked high interest in this context because of their ability to efficiently generate heat upon light excitation through a resonance process called plasmon resonance.[6,7] This photothermal effect, known as the thermoplasmonic effect,[8,9] is triggered as soon as the nanoparticles are irradiated, and benefits from spectral tunability (by tailoring the size and/or morphology of the nanoparticles) and insensitivity to the surrounding environment in which the nanoparticles are dispersed, resulting in a robust spatiotemporal control of heating. These properties have naturally led to an increasing use of AuNPs for temperature control at the nano-/microscale, specifically for photothermal therapy,[10,11] and thermoresponsive drug release from microcapsules.[12,13] For such biologically oriented applications, it remains crucial to precisely quantify the temperature gradients that are generated in the vicinity of AuNPs upon light excitation. However, the spatial resolution of standard thermometers is obviously not adapted to capture nano- and microscale temperature fields/gradients,[14] and more advanced sensing techniques are thus required for that purpose.[15,16]

So far, *in situ* microscale quantification of thermoplasmonic heating has been essentially based on the measurement of temperature-dependent fluorescence properties of additional extrinsic reporters (fluorophore molecules or particles). These properties include intensity,[17−19] lifetime,[20,21] variation of spectrum,[22] and anisotropy.[23,24] However, an appropriate calibration is required to estimate the local temperature from the measurement of variations in such properties. The use of fluorescent reporters may also suffer from photo- or thermobleaching that biases the temperature quantification,[25] and it may also affect the chemical environment of the system under study. As an alternative to fluorescence measurements, quantitative phase imaging turns out to be relevant for temperature mapping in sensitive environments, because measuring the phase of light is label-free, noninvasive, and highly sensitive to temperature variations.[26] Indeed, temperature gradients generated by thermoplasmonic heating result in variations of refractive index in the surrounding medium, which in turn imprint a phase delay, or equivalently a wavefront distortion, on light passing through the sample. By recording wavefront distortions, we can thus quantify and map the temperature rise generated *in situ* by AuNPs.[27,28]

Cross-grating wavefront microscopy (CGM)[29−31] is a technique based on quadriwave lateral shearing interferometry[32] that has several advantages: it is simple, compact, and poorly sensitive to environmental perturbations. It also benefits from high signal/noise ratio and high spatiotemporal

Received: September 11, 2023
Revised: December 2, 2023
Accepted: December 5, 2023

https://doi.org/10.1021/acs.jpclett.3c02550
J. Phys. Chem. Lett. 2023, 14, 11200−11207

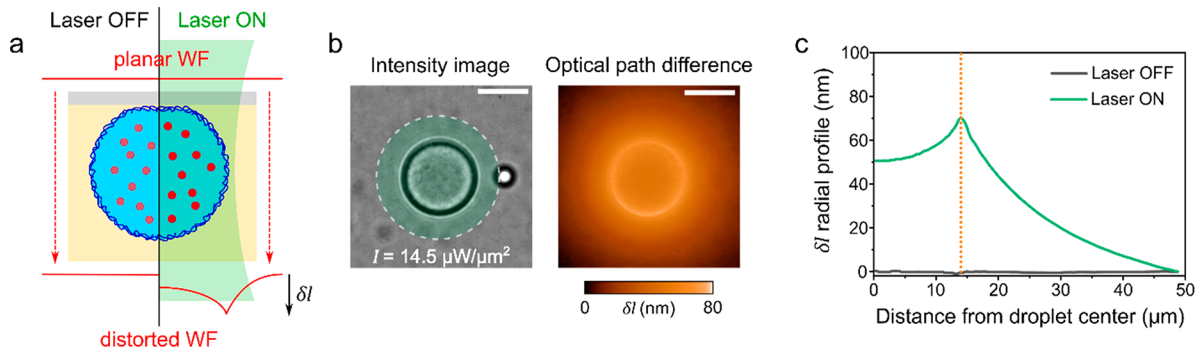

Figure 1. Experimental measurement of wavefront distortion in droplets loaded with gold nanoparticles (AuNPs) during thermoplasmonic heating. (a) Optical path difference (δl) imprinted to a planar wavefront (WF, red solid line) after propagation (from top to bottom, dashed red arrows) across a droplet loaded with AuNPs (red dots) and stabilized by a polymer shell (deep blue envelope), exposed or not to laser irradiation (green beam). (b) Typical intensity image of a droplet (left) and the corresponding δl signature of thermoplasmonic heating (right) provided by cross-grating microscopy (the excitation laser spot is shown by a green disk). Scale bars = 20 μm. (c) δl radial profiles (azimuthal average) of the droplet shown in b, prior to and during laser irradiation (black and green curves, respectively). The orange dashed line indicates the edge of the droplet (28 μm in diameter).

resolution.[33] CGM provides both intensity and wavefront images of a sample from the analysis of the interferogram produced by a 0−π checkerboard-like diffraction grating placed at a millimeter distance from the sensor of a camera.[30] CGM was successfully implemented to measure temperature fields and heating power densities at the level of single AuNPs or arrays of AuNPs,[27,34] demonstrating the high potential of this technique for *in situ* nanoscale thermometry without resorting to any extrinsic calibration. However, converting wavefront images into quantitative temperature images with this approach relies on the possibility to define a thermal Green's function in the geometry of the nanoparticles' environment. This requirement makes this technique appropriate for simple sample geometries, typically for nanoparticles lying upon a flat interface between two semi-infinite media,[27,34−36] but not for more complex source distributions, in particular for nanoparticles dispersed in three dimensions (e.g., dispersed in a fluid or in microencapsulation systems).

In this article, we demonstrate the capability of CGM to provide label-free *in situ* microscale temperature measurements in polymer microcapsules, prepared under the form of an emulsion of aqueous microdroplets loaded with AuNPs. The calculation of a thermal Green's function for a random (Brownian) three-dimensional distribution of thousands of AuNPs is basically impossible, ruling out the possibility to deduce temperature values in the emulsion droplets. Our approach overcomes this issue by combining CGM measurements and simulation-based inference of heat diffusion around an isolated droplet to determine the temperature values that are reached in the experimental conditions. Briefly, CGM wavefront images of droplets loaded with AuNPs were recorded under exposure to a visible laser light to extract the wavefront distortion due to thermoplasmonic effects. In parallel, the wavefront signature of an isolated heating droplet and the associated temperature field were predicted numerically by solving the steady-state heat equation in the appropriate geometry. Eventually, the heating power dissipated *in situ*, and the temperature effectively reached in the droplet core was inferred from the comparison between experimental and numerical data. This microscale thermometry approach was implemented on droplets of varying diameter and was qualitatively validated *in situ* by probing the heating-induced solubility transition of a thermoresponsive polymer. To our knowledge, this work constitutes the first demonstration of label-free quantitative thermometry in a microscale three-dimensional thermoplasmonic source.

Aqueous droplets loaded with gold nanoparticles (AuNPs) were prepared by emulsification of an aqueous solution containing AuNPs (diameter ∼50 nm) and a cationic copolymer of poly(L-lysine) (PLL) in a fluorinated oil containing an anionic surfactant (Krytox) (see the Experimental Methods section in the Supporting Information). The copolymer (here made of PLL and poly(*N*-isopropylacrylamide, PNIPAM, and denoted PLL-*g*-PNIPAM) was used to form a polymer shell at the surface of the droplets upon emulsification, via spontaneous cation:anion association with Krytox across the water/oil interface,[37−39] hence facilitating the dispersion and stabilization of the droplets (especially against heat-induced coalescence).

Intensity and wavefront images of the emulsion droplets were recorded with the cross-grating wavefront microscopy (CGM) setup depicted in Figure S1. The imaging beam (wavelength of 625 nm) was propagating from top to bottom along the z axis, the assumption of straight-line propagation being essentially valid in the continuous oil phase (in absence of droplet) and for light passing through the upper cap of the droplets (vertical incidence). By quantitatively measuring wavefront distortions of the imaging beam as it propagates through the sample, CGM allows for a mapping of the optical path difference (denoted as δl) generated by the refractive features of the sample. Indeed, δl corresponds to the integral of the local variations of refractive index $(n(x,y,z) - n_{ref})$ over the sample thickness (where $n(x,y,z)$ is the refractive index of the sample at the position (x,y,z), and n_{ref} is a refractive index of reference usually taken in a homogeneous region of the sample):

$$\delta l(x, y) = \int (n(x, y, z) - n_{ref})\, dz$$

In this work, all the measured δl values were negative (since heating induces a global decrease of the refractive indices) but were inverted and shown as positive values in all figures and graphs in this article for convenience.

The typical δl signature of the droplets under laser irradiation includes two contributions: first, an intrinsic δl due to the difference of refractive indices between the aqueous

https://doi.org/10.1021/acs.jpclett.3c02550
J. Phys. Chem. Lett. 2023, 14, 11200−11207

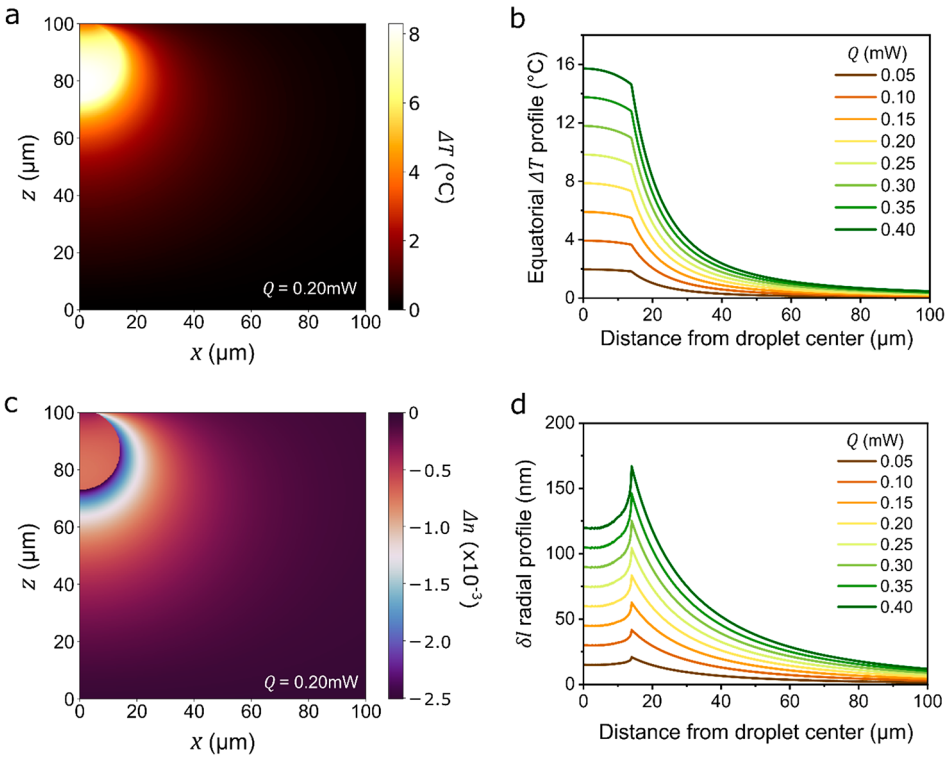

Figure 2. Numerical simulations of δl radial profiles calculated by solving the steady-state heat equation in axisymmetric geometry around a uniform spherical heat source modeling the droplet (28 μm in diameter, corresponding to the droplet in Figure 1). (a) Side-view cross-section map of temperature rise ΔT for a heating power of Q = 0.20 mW. (b) Radial profiles of temperature rise in the equatorial plane of the droplet for different values of heating power used in the simulation. (c) Side-view cross-section map of variation of refractive index Δn for a heating power of Q = 0.20 mW. (d) δl radial profiles calculated by numerical integration of Δn along the z direction, for different values of heating power used in the simulation.

core and the surrounding oil phase, and second, a δl variation due to thermoplasmonic heating, the refractive indices of oil and water varying with temperature (this effect being quantified by dn/dT coefficients). Only the second contribution was of interest to determine the local temperatures upon heating. So, to specifically isolate it and get rid of the first contribution, a reference δl image of the sample was recorded with the laser off (no heating), and was subtracted to δl images that were recorded under laser irradiation (Figure 1).

Note that CGM primarily measures wavefront *gradients*, followed by integration that naturally yields an arbitrary offset on the wavefront image (i.e., on the δl map).[30] This offset does not need to be known to retrieve the temperature profiles since the algorithm is based on the use of $1/r$ Green's functions that impose the final temperature map to be a solution of the Laplace equation. As a convention, when plotting δl radial profiles, we chose to apply an offset so that δl equals zero at a distance of 50 μm from the droplet center (Figure 1c).

Due to complex, nonanalytical patterns of heat diffusion and temperature gradients in the biphasic system sampled here, and due to the offset added to experimental δl values, absolute temperature values could not be directly retrieved from the experimental δl profiles. To get around this issue, the experimental data were compared with numerical data that were generated by simulations of steady-state heat diffusion in the geometry corresponding to an isolated droplet. Assuming that the AuNPs were uniformly distributed within its core, the droplet was assimilated to a uniform spherical heat source delivering a heating power Q. The relevant range of Q values that were used in the simulations (typically a fraction of mW) was determined from an estimation of the power dissipated under the experimental conditions. Details on the simulation procedure are presented in section II.2 in the Supporting Information (including discussions on the choice of the thermal parameters for the droplet and the heating power distribution, and Figures S2−S5).

Figure 2a shows an axisymmetric side-view cross-section map of the temperature rise generated by a 28-μm droplet in its environment (here for Q = 0.20 mW), on a typical length scale of 100 μm corresponding to the internal thickness of the capillary. The radial profiles of temperature rise ΔT in the equatorial plane of the droplet are shown in Figure 2b for different values of the heating power used in the simulation. In first approximation, the droplet was assimilated to pure water, for which $dn/dT = -0.9 \times 10^{-4}$ K^{-1} (the validity of this assumption will be discussed later).[9] The dn/dT coefficient of the oil phase was measured to be -3.16×10^{-4} K^{-1} (see section II.3 and Figure S6 in the Supporting Information). Using these dn/dT values in the simulations, the local temperature rise was converted into the local variation of refractive index (Figure 2c). Eventually, the δl radial profile was calculated by numerically integrating the variations of the refractive index over the sample thickness (Figure 2d). In agreement with the experimental observations, the numerical δl profiles exhibited a maximum located at the boundary of the droplet, resulting from a combination of (i) temperature gradients directed towards the droplet core and (ii) $|dn/dT|$ gradients directed towards the oil phase (as $|dn/dT|_{water} < |dn/dT|_{oil}$).

https://doi.org/10.1021/acs.jpclett.3c02550
J. Phys. Chem. Lett. 2023, 14, 11200−11207

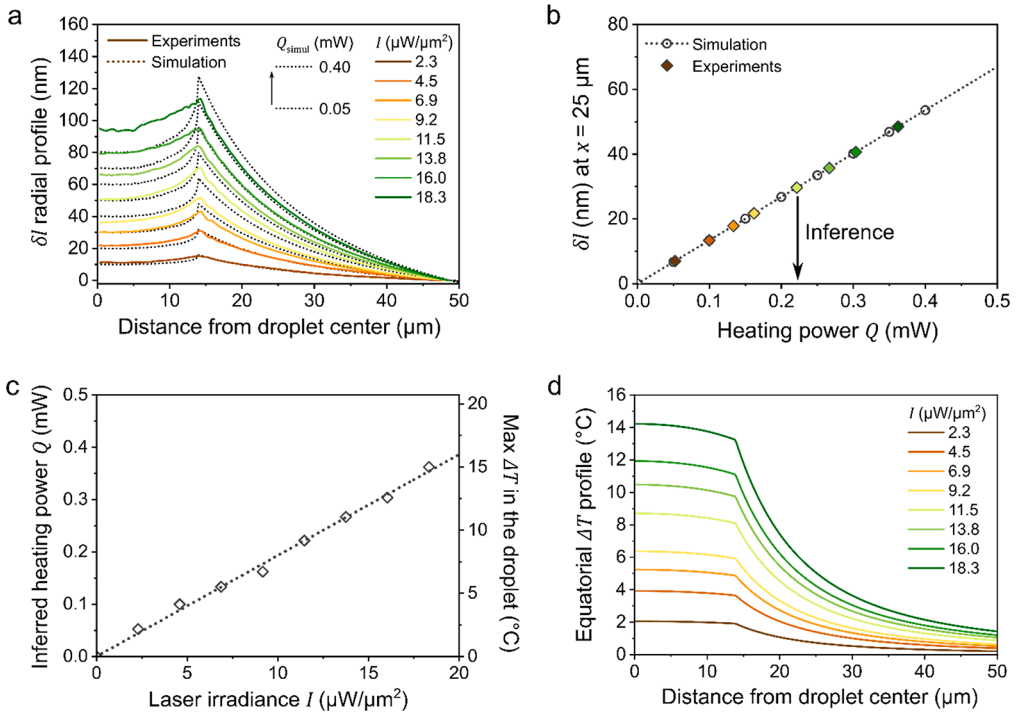

Figure 3. Inference-based thermometry protocol. (a) Comparison between experimental δl profiles (solid lines) and numerical δl profiles (black dashed lines) generated using test values of heating power (between 0.05 and 0.40 mW, with a fixed increment of 0.05 mW from bottom to top). (b) Projection of the experimental δl values measured at 25 μm (colored diamonds) on the curve representing numerical δl values measured at the same position (black open circles) and inference of the heating power reached in the experimental conditions. (c) Simulation-based inferred heating power (Q, left axis) and maximal temperature rise (ΔT, right axis) reached in the droplet core in the different irradiation conditions. (d) Radial profiles of temperature rise in the equatorial plane of the droplet, as deduced from the inference process.

By performing these numerical simulations for different values of the heating power Q, we eventually obtained a direct quantitative correlation between heating power, temperature, and δl values.

By matching the experimental and numerical δl profiles, we were able to infer the heating power that was dissipated in the experimental conditions and then to deduce the temperature that was effectively reached in the droplets. The inference protocol was implemented in the oil region, away from the droplet and the water/oil interface where nonhomogeneities made simulations more demanding (as discussed below). Experimental profiles were recorded for different values of laser irradiance and were shifted to equal zero at the distance of 50 μm from the droplet center (Figure 3a, solid lines). Numerical δl profiles were simulated for different heating powers (regularly spaced between 0.05 and 0.40 mW), and similarly shifted to zero at the same 50-μm distance from the droplet center (Figure 3a, dashed lines). Then, the δl values measured on the numerical profiles were used as an intrinsic δl/heating power calibration. This is illustrated in Figure 3b where the δl values measured at the arbitrarily chosen position of 25 μm from the droplet center are reported as a function of the heating powers tested in the simulations. The projection of the experimental δl values (measured at the same 25-μm position) on this calibration curve enabled us to infer the heating power that was effectively dissipated in the experiments (Figures 3b and 3c, left axis). When the appropriate values of heating power were implemented in the simulations, the calculated numerical δl decay nicely fitted the experimental decay observed in the oil phase (see Figure S8 in the Supporting Information). Eventually, using the correlation between the heating power and temperature provided by the simulations (Figure 2b), we could deduce the temperature increase reached in the droplet core (Figure 3c, right axis). For the droplet under study in Figures 1−3 (28 μm in diameter), a maximum increase by +15 °C was, for instance, estimated at the highest tested irradiance of ∼18 μW/μm^2. Figure 3d shows the inferred profiles of temperature rise in the equatorial plane of the droplet for the different laser irradiances tested (note that, as revealed in the ΔT map in Figure 2a, the maximum temperature was not reached in the equatorial plane but slightly below due to the presence of the capillary on top of the droplet).

We used that inference-based thermometry protocol on droplets of different sizes to determine the maximum temperature values reached in the droplets at different laser irradiances (Figure 4a). Interestingly, the data collapsed on the same linear curve when plotting the temperature rise (with respect to room temperature, 22 °C) normalized by the square of the droplet radius as a function of the laser irradiance, as shown in Figure 4b. In other words, the temperature rise scales with the square of the droplet radius. This trend is consistent with the theoretical prediction we derived in section II.4 in the Supporting Information. In addition, the dispersion of the data around the mean values for that scaling law (see the inset in Figure 4b) allowed us to estimate an overall error on our temperature determination, which was less than 8% (corresponding to the maximum amplitude of the error bars). When associated with temperature rises of up to 15 °C, this error can thus be estimated to be ∼1 °C, which is in agreement with the original work using CGM for thermal imaging.[27] This rough estimation includes all the sources of error of our protocol

https://doi.org/10.1021/acs.jpclett.3c02550
J. Phys. Chem. Lett. 2023, 14, 11200−11207

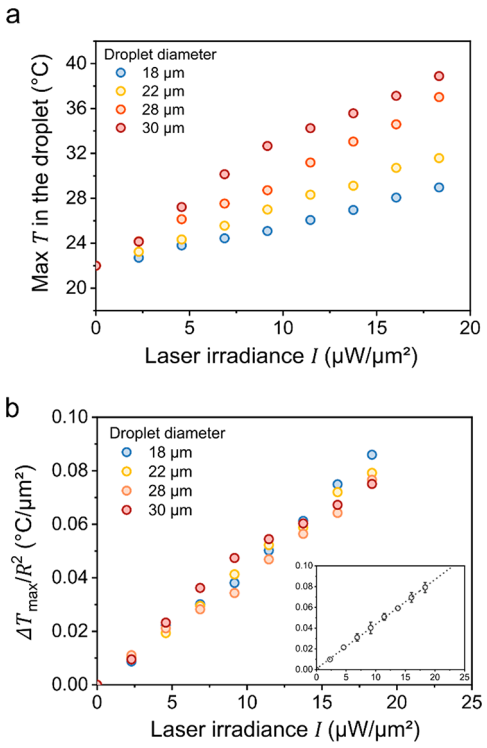

Figure 4. (a) Absolute maximal temperature reached in the droplet core, as deduced from the inference process, for droplets of different sizes (room temperature was set to 22 °C). (b) Evolution of the (maximum) temperature rise normalized by the square of the droplet radius as a function of the laser irradiance for droplets of different sizes. Inset: Plot of the mean value for each irradiance (the error bars correspond to the standard deviations and the dashed line is a linear fit).

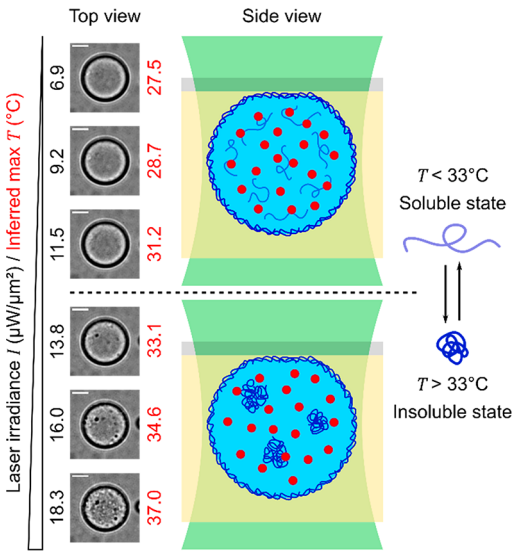

Figure 5. Intensity imaging of the precipitation of excess PLL-*g*-PNIPAM (deep blue chains) in the core of the droplet under study in Figure 1−3, above a threshold laser irradiance of 13.8 $\mu W/\mu m^2$. According to our thermometry protocol, this irradiance was associated with a temperature of 33.1 °C, which corresponds to the cloud point of PLL-*g*-PNIPAM, i.e., the temperature where it becomes poorly soluble in water. Scale bar in the intensity micrographs is 10 μm.

(listed in section II.5 in the Supporting Information), for which a rigorous propagation of uncertainty was not straightforward.

To get a qualitative validation of this thermometry approach, we leveraged the thermoresponsive properties of the PNIPAM strands in the PLL-*g*-PNIPAM copolymer used to form the shell around the droplet. Indeed, PNIPAM is a polymer that exhibits a lower critical solution temperature (LCST) of 32−33 °C, above which it becomes poorly soluble in water.[40] Interestingly, this behavior was also observed at the same critical temperature for the PLL-*g*-PNIPAM copolymer,[38] as revealed by turbidimetry (see section II.6 and Figure S7 in the Supporting Information). Accordingly, crossing this threshold temperature of 33 °C in droplets loaded with PLL-*g*-PNIPAM would be revealed by the formation of a polymer precipitate (so-called "cloud point"), hence providing a qualitative confirmation of the efficiency of thermoplasmonic heating in the droplets. Visible granulation however would require the presence of a large excess PLL-*g*-PNIPAM in bulk, i.e., at a concentration that oversaturates the water/oil interface (typically 20 g/L in droplet of diameter about 25 μm), so that residual polymer chains remaining in the droplet core could precipitate.

Figure 5 shows intensity micrographs of the droplet under study in Figures 1−3 (28 μm in diameter, loaded with 20 g/L PLL-*g*-PNIPAM) under increasing laser irradiance and the corresponding maximum temperature reached in the droplet core as predicted by our thermometry method. Above an irradiance of 13.8 $\mu W/\mu m^2$, a loss of solubility of PLL-*g*-PNIPAM, betrayed by the formation of granules in the droplet core, was observed. The temperature associated with this irradiation condition was predicted to be 33.1 °C, effectively matching with the cloud point of PLL-*g*-PNIPAM, hence confirming the predictability and precision of our thermometry protocol.

The final step of our inference protocol was to retrieve the effective values of dn/dT in the droplet. Indeed, in the simulations, we chose a constant and uniform dn/dT coefficient for the aqueous phase, equal to that of pure water. This simplified (and necessarily wrong) estimation is responsible for the discrepancy between the experimental and numerical δl values in the droplet region (Figure S8). However, it did not impede or bias our thermometry protocol since the temperature fields wereinferred from the thermal signature in the homogeneous bulk oil region (for which the optical and thermal properties are well characterized), and the dn/dT coefficient of the aqueous phase never came into account in that inference protocol. However, knowing the effective dn/dT of a complex medium in a confined geometry can be of interest by itself.

The actual dn/dT coefficient in the droplet was not easy to predict, essentially due to two issues: first, rationalizing the effects of composition heterogeneities, including the formation of polymer granules above the cloud point, on the local and global dn/dT is not an easy task. Second, potential optical aberrations due to the droplet curvature, which may modify the apparent dn/dT, could not be captured in the numerical data since the optical properties of the water/oil interface, such as the reflectivity, were not taken into account in the simulations. To improve the droplet modeling and capture the phenomena mentioned above, we calculated effective dn/dT profiles in the droplet core from the mismatch between experimental and numerical δl values in the droplet region. This protocol is described in section II.7 in Supporting Information (including Figures S9 and **S10**) and was applied

https://doi.org/10.1021/acs.jpclett.3c02550
J. Phys. Chem. Lett. 2023, 14, 11200−11207

to droplets of different sizes, resulting in the effective dn/dT radial profiles that are shown in Figure 6a.

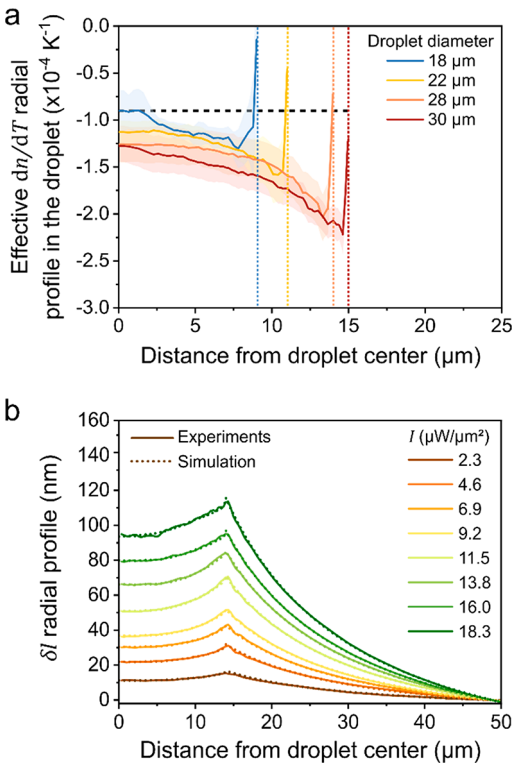

Figure 6. (a) Effective dn/dT radial profiles measured in droplets of different sizes upon thermoplasmonic heating. The solid lines represent the average profiles over the different irradiation conditions, and the envelope of the curves represents the variability due to heating. The horizontal black dashed line represents the dn/dT value for pure bulk water. The vertical dashed lines indicate the edges of the droplets. (b) Superimposition of experimental δl profiles (solid lines) and optimal numerical profiles (dashed lines) for the 28-μm droplet under study in Figures 1−3.

For all droplet sizes, the effective dn/dT profiles exhibited a consistent decrease from the center of the droplets towards their edge. These gradients can be reasonably attributed to spherical aberrations associated with the curvature of the droplet and not to the nonuniform polymer distribution since the same profile shapes were also observed in droplets containing no polymer (Figure S10a,b). In addition, the absolute values of effective dn/dT in the droplet were systematically higher than that of pure water, and increased with temperature (Figure S10 and envelopes in Figure 6a), suggesting that the refractive properties of water were modified by the presence of the thermosensitive PLL-g-PNIPAM (this point is further discussed in section II.8 and Figures S11−S12 in the Supporting Information). Interestingly, the effective dn/dT became closer to that of pure water and showed less sensitivity to temperature as the size of the droplet decreased, likely because smaller droplets (with higher surface/volume ratio) contained significantly lower bulk concentrations of PLL-g-PNIPAM due to the sequestration/immobilization of most of the polymer in the shell formed at the periphery of the droplets.[38]

Eventually, CGM was used to estimate not only the temperature rise but also the effective dn/dT profile within the droplet cores. Using the appropriate values of heating power and dn/dT in the simulations, the experimental δl profiles could be perfectly fitted with numerical profiles as shown in Figure 6b for the droplet under study in Figure 1−3.

In summary, this work introduces a label-free thermometry method that enables the *in situ* characterization of photothermal properties of microdroplets kept under exposure to light, namely temperature distribution, delivered heating power and values of dn/dT coefficient. This thermometry approach is general, since it relies on the measurement of heat-induced variations of optical path difference (δl) using cross-grating wavefront microscopy coupled with geometry-dependent simulations of the expected temperature gradients. This approach was validated on the particular model of aqueous-core emulsion microdroplets loaded with thousands of gold nanoparticles, which is representative of several encapsulation systems and for which the thermoplasmonic-induced δl signature cannot be straightforwardly converted into temperature values using analytical tools. δl variations were fairly predicted by numerical simulations of steady-state heat transfers, enabling a robust inference of the experimental temperature fields, with a precision of ∼1 °C. In addition, when the droplets were loaded with an extrinsic thermosensitive probe, namely, an excess of the thermoresponsive PLL-g-PNIPAM polymer, the threshold irradiance above which the polymer loses its solubility and forms observable microaggregates (indicating T > 33 °C) was correctly predicted, confirming the potential of our protocol for accurate *in situ* thermometry.

Since our method is based on a noninvasive measurement of δl signatures in the uniform environment surrounding the plasmonic source (here the oil phase surrounding the droplets), it does not depend on the composition (and potential heterogeneities) of the plasmonic source itself and does not require internal probes. We thus believe that this thermometry approach could be applied to a variety of three-dimensional thermoplasmonic systems, whose geometry can be numerically simulated. It accordingly holds potential not only to measure temperatures in AuNPs-loaded microgels or vesicles, which are of interest for encapsulation and/or drug delivery applications[41,42] or for the design of artificial cells,[43,44] but also to investigate thermophoretic colloidal systems such as thermoplasmonic microswimmers.[45] Associated with tomography, our approach could also be extended to more complex and/or dynamic geometries, such as living cells loaded with nanoheaters.[46]

■ ASSOCIATED CONTENT

Supporting Information

Supporting Information contain The Supporting Information is available free of charge at https://pubs.acs.org/doi/10.1021/acs.jpclett.3c02550.

Detailed Experimental Methods (including the synthesis and thermal characterization of PLL-g-PNIPAM, the formulation of the emulsions, and details on the wavefront microscopy setup), and Figures S1−S12 accompanied by supplementary comments and discussions (including details and discussions on the simulation procedure, discussions on the precision on thermometry protocol, the measurement of the dn/dT coefficients of the bulk oil and aqueous phases, and the protocol for determining the effective dn/dT profiles in the droplet) (PDF)

https://doi.org/10.1021/acs.jpclett.3c02550
J. Phys. Chem. Lett. 2023, 14, 11200−11207

AUTHOR INFORMATION

Corresponding Authors

Lucas Sixdenier − *PASTEUR, Département de chimie, École normale supérieure, PSL University, Sorbonne Université, CNRS, 75005 Paris, France;* Present Address: Center for Soft Matter Research, New York University, New York, NY 10003; orcid.org/0000-0002-7085-0970; Email: ls6166@nyu.edu

Emmanuelle Marie − *PASTEUR, Département de chimie, École normale supérieure, PSL University, Sorbonne Université, CNRS, 75005 Paris, France;* Email: emmanuelle.marie@ens.psl.eu

Authors

Guillaume Baffou − *Institut Fresnel, CNRS, Aix Marseille University, 13013 Marseille, France;* orcid.org/0000-0003-0488-1362

Christophe Tribet − *PASTEUR, Département de chimie, École normale supérieure, PSL University, Sorbonne Université, CNRS, 75005 Paris, France;* orcid.org/0000-0002-5953-0968

Complete contact information is available at: https://pubs.acs.org/10.1021/acs.jpclett.3c02550

Notes

The authors declare no competing financial interest.

ACKNOWLEDGMENTS

This work was supported by the following institutions and programs: the DYNAMO Laboratory of Excellence (ANR-11-LABEX-0011-01); the Agence Nationale pour la Recherche (ANR-20-CE06-0007 Fliposomes and ANR-17-CE09-0019 CASCADE); and Sorbonne University (Ecole Doctorale 388 scholarship). We thank Ludovic Jullien for seminal discussions, including on thermo-fluorimetry; Sadman Shakib for the measurement of the refractive index of the oil phase; and Victor Chardès for his valuable insights into numerical methods.

REFERENCES

(1) Sharifi, M.; Attar, F.; Saboury, A. A.; Akhtari, K.; Hooshmand, N.; Hasan, A.; El-Sayed, M. A.; Falahati, M. Plasmonic Gold Nanoparticles: Optical Manipulation, Imaging, Drug Delivery and Therapy. *J. Controlled Release* **2019**, *311*−*312*, 170−189.

(2) Zhang, H.; Xia, H.; Zhao, Y. Optically Triggered and Spatially Controllable Shape-Memory Polymer-Gold Nanoparticle Composite Materials. *J. Mater. Chem.* **2012**, *22*, 845−849.

(3) Pastoriza-Santos, I.; Kinnear, C.; Pérez-Juste, J.; Mulvaney, P.; Liz-Marzán, L. M. Plasmonic Polymer Nanocomposites. *Nat. Rev. Mater.* **2018**, *3*, 375−391.

(4) Zhang, A.; Jung, K.; Li, A.; Liu, J.; Boyer, C. Recent Advances in Stimuli-Responsive Polymer Systems for Remotely Controlled Drug Release. *Prog. Polym. Sci.* **2019**, *99*, No. 101164.

(5) Kauscher, U.; Holme, M. N.; Björnmalm, M.; Stevens, M. M. Physical Stimuli-Responsive Vesicles in Drug Delivery: Beyond Liposomes and Polymersomes. *Adv. Drug Delivery Rev.* **2019**, *138*, 259−275.

(6) Brongersma, M. L.; Halas, N. J.; Nordlander, P. Plasmon-Induced Hot Carrier Science and Technology. *Nat. Nanotechnol.* **2015**, *10*, 25−34.

(7) Amendola, V.; Pilot, R.; Frasconi, M.; Maragò, O. M.; Iatì, M. A. Surface Plasmon Resonance in Gold Nanoparticles: A Review. *J. Phys.: Condens. Matter* **2017**, *29*, No. 203002.

(8) Baffou, G.; Quidant, R. Thermo-Plasmonics: Using Metallic Nanostructures as Nano-Sources of Heat. *Laser Photonics Rev.* **2013**, *7*, 171−187.

(9) Baffou, G. *Thermoplasmonics: Heating Metal Nanoparticles Using Light*; Cambridge University Press: 2017.

(10) Cai, K.; Zhang, W.; Zhang, J.; Li, H.; Han, H.; Zhai, T. Design of Gold Hollow Nanorods with Controllable Aspect Ratio for Multimodal Imaging and Combined Chemo-Photothermal Therapy in the Second Near-Infrared Window. *ACS Appl. Mater. Interfaces* **2018**, *10*, 36703−36710.

(11) Wu, Y.; Ali, M. R. K.; Dong, B.; Han, T.; Chen, K.; Chen, J.; Tang, Y.; Fang, N.; Wang, F.; El-Sayed, M. A. Gold Nanorod Photothermal Therapy Alters Cell Junctions and Actin Network in Inhibiting Cancer Cell Collective Migration. *ACS Nano* **2018**, *12*, 9279−9290.

(12) Song, J.; Fang, Z.; Wang, C.; Zhou, J.; Duan, B.; Pu, L.; Duan, H. Photolabile Plasmonic Vesicles Assembled from Amphiphilic Gold Nanoparticles for Remote-Controlled Traceable Drug Delivery. *Nanoscale* **2013**, *5*, 5816−5824.

(13) Shao, J.; Xuan, M.; Si, T.; Dai, L.; He, Q. Biointerfacing Polymeric Microcapsules for in Vivo Near-Infrared Light-Triggered Drug Release. *Nanoscale* **2015**, *7*, 19092−19098.

(14) Richardson, H. H.; Carlson, M. T.; Tandler, P. J.; Hernandez, P.; Govorov, A. O. Experimental and Theoretical Studies of Light-to-Heat Conversion and Collective Heating Effects in Metal Nanoparticle Solutions. *Nano Lett.* **2009**, *9*, 1139−1146.

(15) Quintanilla, M.; Liz-Marzán, L. M. Guiding Rules for Selecting a Nanothermometer. *Nano Today* **2018**, *19*, 126−145.

(16) Baffou, G.; Bordacchini, I.; Baldi, A.; Quidant, R. Simple Experimental Procedures to Distinguish Photothermal from Hot-Carrier Processes in Plasmonics. *Light Sci. Appl.* **2020**, *9*, 108.

(17) Chiu, M. J.; Chu, L. K. Quantifying the Photothermal Efficiency of Gold Nanoparticles Using Tryptophan as an in Situ Fluorescent Thermometer. *Phys. Chem. Chem. Phys.* **2015**, *17*, 17090−17100.

(18) Bendix, P. M.; Reihani, S. N. S.; Oddershede, L. B. Direct Measurements of Heating by Electromagnetically Trapped Gold Nanoparticles on Supported Lipid Bilayers. *ACS Nano* **2010**, *4*, 2256−2262.

(19) Ebrahimi, S.; Akhlaghi, Y.; Kompany-Zareh, M.; Rinnan, Å. Nucleic Acid Based Fluorescent Nanothermometers. *ACS Nano* **2014**, *8*, 10372−10382.

(20) Coppens, Z. J.; Li, W.; Walker, D. G.; Valentine, J. G. Probing and Controlling Photothermal Heat Generation in Plasmonic Nanostructures. *Nano Lett.* **2013**, *13*, 1023−1028.

(21) Freddi, S.; Sironi, L.; D'Antuono, R.; Morone, D.; Donà, A.; Cabrini, E.; D'Alfonso, L.; Collini, M.; Pallavicini, P.; Baldi, G.; Maggioni, D.; Chirico, G. A Molecular Thermometer for Nanoparticles for Optical Hyperthermia. *Nano Lett.* **2013**, *13*, 2004−2010.

(22) Aigouy, L.; Tessier, G.; Mortier, M.; Charlot, B. Scanning Thermal Imaging of Microelectronic Circuits with a Fluorescent Nanoprobe. *Appl. Phys. Lett.* **2005**, *87*, 1−3.

(23) Baffou, G.; Kreuzer, M. P.; Kulzer, F.; Quidant, R. Temperature Mapping near Plasmonic Nanostructures Using Fluorescence Polarization Anisotropy. *Opt. Express* **2009**, *17*, 3291.

(24) Donner, J. S.; Thompson, S. A.; Kreuzer, M. P.; Baffou, G.; Quidant, R. Mapping Intracellular Temperature Using Green Fluorescent Protein. *Nano Lett.* **2012**, *12*, 2107−2111.

(25) Bradac, C.; Lim, S. F.; Chang, H. C.; Aharonovich, I. Optical Nanoscale Thermometry: From Fundamental Mechanisms to Emerging Practical Applications. *Adv. Opt. Mater.* **2020**, *8*, 1−29.

(26) Blum, O.; Shaked, N. T. Prediction of Photothermal Phase Signatures from Arbitrary Plasmonic Nanoparticles and Experimental Verification. *Light Sci. Appl.* **2015**, *4*, e322.

(27) Baffou, G.; Bon, P.; Savatier, J.; Polleux, J.; Zhu, M.; Merlin, M.; Rigneault, H.; Monneret, S. Thermal Imaging of Nanostructures by Quantitative Optical Phase Analysis. *ACS Nano* **2012**, *6*, 2452−2458.

(28) Oh, J.; Lee, G. H.; Rho, J.; Shin, S.; Lee, B. J.; Nam, Y.; Park, Y. Optical Measurements of Three-Dimensional Microscopic Temper-

ature Distributions Around Gold Nanorods Excited by Localized Surface Plasmon Resonance. *Phys. Rev. Appl.* **2019**, *11*, 1.
(29) Bon, P.; Maucort, G.; Wattellier, B.; Monneret, S. Quadriwave Lateral Shearing Interferometry for Quantitative Phase Microscopy of Living Cells. *Opt. Express* **2009**, *17*, 13080.
(30) Baffou, G. Quantitative Phase Microscopy Using Quadriwave Lateral Shearing Interferometry (QLSI): Principle, Terminology, Algorithm and Grating Shadow Description. *J. Phys. D. Appl. Phys.* **2021**, *54*, No. 294002.
(31) Baffou, G. Wavefront Microscopy Using Quadriwave Lateral Shearing Interferometry: From Bioimaging to Nanophotonics. *ACS Photonics* **2023**, *10*, 322−339.
(32) Primot, J.; Guérineau, N. Extended Hartmann Test Based on the Pseudoguiding Property of a Hartmann Mask Completed by a Phase Chessboard. *Appl. Opt.* **2000**, *39*, 5715.
(33) Marthy, B.; Baffou, G. Cross-Grating Phase Microscopy (CGM): In-Silico Experiments, Noise and Accuracy. *Opt. Commun.* **2022**, *521*, No. 128577.
(34) Baffou, G.; Berto, P.; Bermúdez Ureña, E.; Quidant, R.; Monneret, S.; Polleux, J.; Rigneault, H. Photoinduced Heating of Nanoparticle Arrays. *ACS Nano* **2013**, *7*, 6478−6488.
(35) Bon, P.; Belaid, N.; Lagrange, D.; Bergaud, C.; Rigneault, H.; Monneret, S.; Baffou, G. Three-Dimensional Temperature Imaging around a Gold Microwire. *Appl. Phys. Lett.* **2013**, *102*, 1−5.
(36) Berto, P.; Philippet, L.; Osmond, J.; Liu, C. F.; Afridi, A.; Montagut Marques, M.; Molero Agudo, B.; Tessier, G.; Quidant, R. Tunable and Free-Form Planar Optics. *Nat. Photonics* **2019**, *13*, 649−656.
(37) Zhang, J.; Coulston, R. J.; Jones, S. T.; Geng, J.; Scherman, O. A.; Abell, C. One-Step Fabrication of Supramolecular Microcapsules from Microfluidic Droplets. *Science* **2012**, *335*, 690−694.
(38) Sixdenier, L.; Tribet, C.; Marie, E. Emulsion-Templated Poly(N-Isopropylacrylamide) Shells Formed by Thermo-Enhanced Interfacial Complexation. *Adv. Funct. Mater.* **2021**, *31*, No. 2105490.
(39) Sixdenier, L.; Augé, A.; Zhao, Y.; Marie, E.; Tribet, C. UCST-Type Polymer Capsules Formed by Interfacial Complexation. *ACS Macro Lett.* **2022**, *11*, 651−656.
(40) Pasparakis, G.; Tsitsilianis, C. LCST Polymers: Thermoresponsive Nanostructured Assemblies towards Bioapplications. *Polymer* **2020**, *211*, No. 123146.
(41) Zhao, J.; Su, H.; Vansuch, G. E.; Liu, Z.; Salaita, K.; Dyer, R. B. Localized Nanoscale Heating Leads to Ultrafast Hydrogel Volume-Phase Transition. *ACS Nano* **2019**, *13*, 515−525.
(42) Amstad, E.; Kim, S. H.; Weitz, D. A. Photo- and Thermoresponsive Polymersomes for Triggered Release. *Angew. Chem.* **2012**, *51*, 12499−12503.
(43) Chen, Z.; De Queiros Silveira, G.; Ma, X.; Xie, Y.; Wu, Y. A.; Barry, E.; Rajh, T.; Fry, H. C.; Laible, P. D.; Rozhkova, E. A. Light-Gated Synthetic Protocells for Plasmon-Enhanced Chemiosmotic Gradient Generation and ATP Synthesis. *Angew. Chemie - Int. Ed.* **2019**, *58*, 4896−4900.
(44) Su, J.; Chen, H.; Xu, Z.; Wang, S.; Liu, X.; Wang, L.; Huang, X. Near-Infrared-Induced Contractile Proteinosome Microreactor with a Fast Control on Enzymatic Reactions. *ACS Appl. Mater. Interfaces* **2020**, *12*, 41079−41087.
(45) Fränzl, M.; Muiños-Landin, S.; Holubec, V.; Cichos, F. Fully Steerable Symmetric Thermoplasmonic Microswimmers. *ACS Nano* **2021**, *15*, 3434−3440.
(46) Li, M.; Lohmüller, T.; Feldmann, J. Optical Injection of Gold Nanoparticles into Living Cells. *Nano Lett.* **2015**, *15*, 770−775.

https://doi.org/10.1021/acs.jpclett.3c02550
J. Phys. Chem. Lett. 2023, 14, 11200−11207